A Topology-Morphing Series Resonant Converter for Photovoltaic Module Applications

Grigorios Sergentanis, Liliana de Lillo, Lee Empringham, C. Mark Johnson
The University of Nottingham
University Park, NG7 2RD
Nottingham, UK
Tel.: +44 / (115) – 8468840.
E-Mail: grigorios.sergentanis@nottingham.ac.uk
URL: http://www.nottingham.ac.uk

Acknowledgements

Keywords

«Resonant Converter», «Boost», «Photovoltaic», «DC-DC converter», «Efficiency»

Abstract

Residential solar photovoltaic (PV) installations frequently use power optimizers to increase their energy production. In this application, the ability to regulate a wide range of voltage with high efficiency is highly desirable. Thus, this paper proposes a novel hybrid-controlled series resonant converter (SRC) for photovoltaic power optimizers. The converter utilizes the advantage of GaN devices, which have improved switching transition times compared to Si devices, hence providing a lower switching loss. Regulation is achieved with fixed-frequency PWM control on the secondary side, while ZVS and ZCS of the devices are achieved with the proposed resonant tank design. The proposed converter maintains high efficiency over a wide voltage range, making the PV system shade-tolerant while keeping the number of switching devices low. The paper presents the operating principles, the design methodology, and simulation results. The results show a high efficiency over a wide voltage range, as well as a wide load range.

Introduction

Due to the nonlinear nature of photovoltaic (PV) panels, to harvest the maximum amount of energy, a maximum power point tracking (MPPT) algorithm is required [1]. This algorithm measures the PV side voltage and current and then gives a reference input voltage for the interfacing converter. This control is normally enacted on a string or array of PV panels, but with the rise of residential installations, module-level power electronics (MPLE) have become a viable option in the form of a dc power optimizer or a microinverter. A PV installation using MPLE has the benefits of high scalability, decreased magnetics size, zero mismatch loss between panels, and increased reliability [2]. DC power optimizers may also be used in building-integrated PV systems, where using a DC microgrid is financially attractive [3]. One of the difficulties in implementing a DC power optimizer is the need to accommodate a wide range of PV voltages, as environmental conditions like insolation, temperature and shading may vary the optimum voltage greatly.

In this work, the authors propose a DC power optimizer that can be used as the first stage in a microinverter, or as a standalone solution that may be connected to a central inverter or DC microgrid. The proposed converter, as seen in Fig. 1, consists of the highly efficient series resonant converter (SRC), used to provide galvanic isolation and voltage step-up via its transformer. On the rectifying full

bridge, the lower diodes are replaced by active switches. These switches are used to achieve input voltage regulation as well as topology morphing. Under typical conditions, the two switches are phase-shift modulated to provide the equivalent function as a boost converter integrated into the SRC. In heavily shaded conditions, where the desired voltage can be quite low, one of the switches is set constantly ON, morphing the rectifying side into a Greinacher voltage doubling circuit, while the other switch is PWM modulated to control the input voltage. The concept of integrating a boost converter with an SRC has been successfully explored by researchers [4], [5], but their regulation range is limited due to duty cycle constraints. The concept of using a topology morphing rectifier to increase the regulation range is also well known [6], but comes at the cost of increased semiconductor devices. The novelty of this research is those two ideas are combined in a converter that does not require additional devices to operate. Another advantage of this converter is that it operates with a fixed switching frequency, allowing more freedom in the transformer design compared with frequency-modulated resonant converters. The latter, such as the LLC converter, have an inherent disadvantage by requiring specific ratios of resonant inductance to magnetizing inductance, limiting the achievable efficiencies [7]. Furthermore, researchers have developed other attractive topologies in the field of micro converters, such as the quasi-Z source SRC converter [8] and converters with switched capacitor/inductor cells [9], however, these solutions require increased magnetic component count, which may pose a problem in terms of volumetric density, if trying to integrate the DC optimizer with the PV panel.

Topology of the Converter

As seen in Fig. 1, the PV panel is connected directly to the input, and an input capacitance is inserted in parallel to stabilize the input voltage to suppress oscillations around the MPP and thereby improve the panel's utilization ratio [10]. The full-bridge created by $S_1 - S_4$ provides the AC voltage to be fed to the transformer. The transformer itself is designed so that its magnetizing inductance provides zero voltage switching (ZVS) on the primary side. The resonant tank, comprised of L_r and C_r is designed so that their resonant frequency is slightly higher than the converter's operating frequency, guaranteeing zero current switching (ZCS) at the secondary bridge (D_1, D_2, S_5, S_6). The resonant inductance may be integrated with the transformer design, or it may be an external inductor in series with the transformer's leakage inductance, depending on the designing switching frequency and the designer's priorities. C_{out} is assumed to be much larger compared to C_r during the converter analysis, and the output of the converter can be a fixed voltage DC microgrid or the DC link of a two-stage inverter system. In either case, the output voltage is assumed constant, as even in the latter scenario, the control of the DC-link voltage is normally encased in the inverter circuit [11]. The converter may operate as a DC transformer (DCX) when the normalized voltage gain is equal to one, and in the boosting mode or the Greinacher mode when the MPP voltage is reduced.
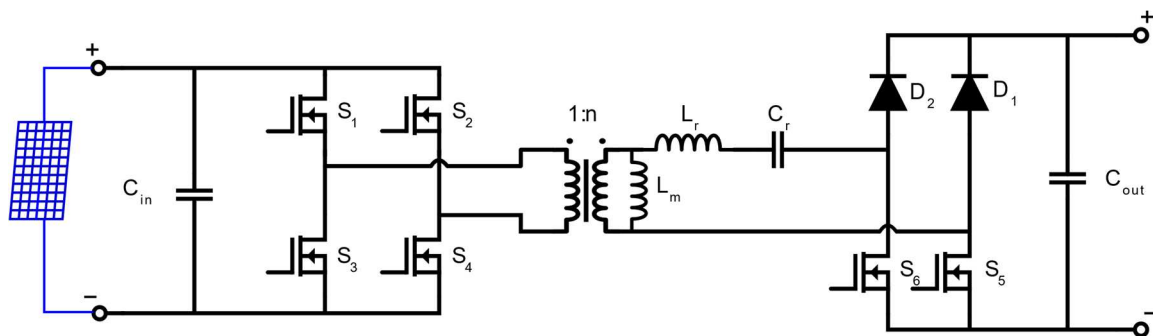

Fig. 1: The proposed converter

DCX operation

At the nominal input voltage, the converter operates as an SRC. This is the highest efficiency state, as energy is transferred from the source to the output for nearly all the operating period. As seen in Fig. 2(a), the current flowing through the resonant branch is sinusoidal. The switching frequency is slightly

lower than the resonant tank's resonant frequency, hence ZCS is guaranteed on D_1, D_2, S_5, S_6 at time t_1. The primary bridge of $S_1 - S_4$ can achieve ZVS turn-on, if the transformer is designed to provide enough magnetizing current during the dead-time interval. For example, during the time $t_1 - t_2$, the voltage transitions on the primary bridge are shown pictorially in Fig. 2(b). The condition to achieve ZVS may be formulated mathematically as:

$$L_m \leq \frac{n^2 t_{dt}}{8 f_s C_{oss}} \qquad (1)$$

With t_{dt} being the dead-time, and C_{oss} the charge equivalent output capacitance of the FETs on the primary bridge. An additional dead-time interval may be added on S_5, S_6 at time t_2, to allow them to also achieve ZVS turn on. Plus, the primary bridge switches turn-off with low losses, as they are conducting only the reflected magnetizing current at the time t_1.
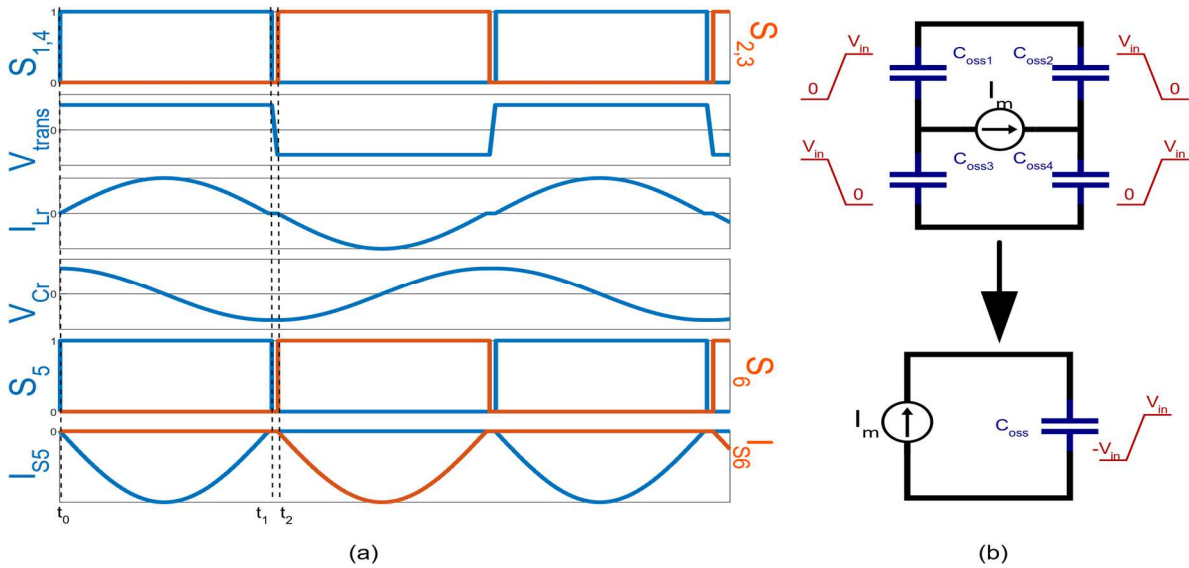

Fig. 2: Operation waveforms at the DCX mode (a), and the equivalent circuit of the full-bridge during the dead-time period (b)

Boosting Operation

When the desired input voltage is lower than the nominal, the converter operates in its boosting mode. This is achieved by adding extra ON time to the switches S_5, S_6 in the form of phase-shifting their respective pulses, as is seen in Fig 3(a). During the overlap of the pulses, the resonant tank is shorted, and L_r is rapidly charged. This results in the secondary side acting as a boost converter operating at double the switching frequency. Afterwards, at $t_1 - t_2$, the current is sinusoidal according to the resonant tank's frequency, hence it will reach zero before time t_3, allowing ZCS for the diodes D_1, D_2. Similar to the DCX mode, in the primary bridge ZVS is achieved by utilizing the dead-time interval, and low turn-off currents are guaranteed as the current in the resonant branch is zero in advance of time t_3. The secondary side switches can still achieve ZVS by adding an additional dead-time delay.

After performing Kirchhoff's laws for each state of the converter, the state plane diagram of the resonant tank can be created, and the converter's gain may be computed geometrically. For the time period $t_0 - t_1$, the following equation describes the trajectory of the resonant tank:

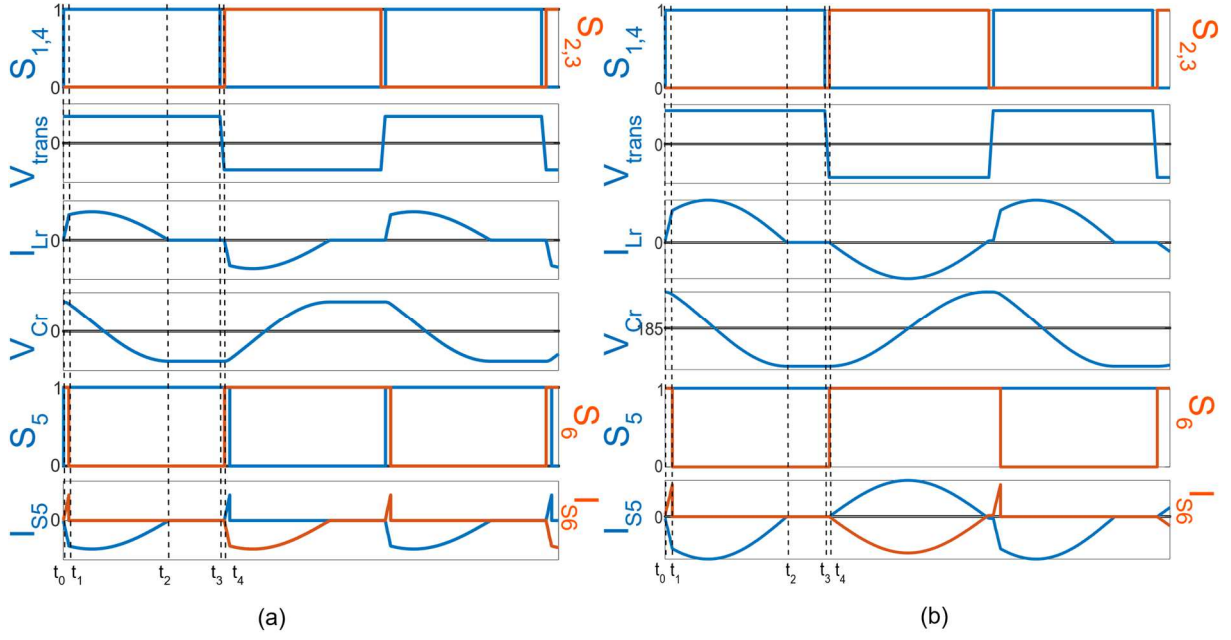$$(v_{cr} - nV_{in})^2 + (Z_r i_{Lr})^2 = (nV_{in} + \Delta v_{cr})^2 \qquad (2)$$

Fig 3: Operation of the converter in the boosting mode (a), and in the Greinacher mode (b).

At the time period $t_1 - t_2$, the respective equation is:

$$(v_{cr} - nV_{in} + V_{out})^2 + (Z_r i_{Lr})^2 = (V_{out} - nV_{in} + \Delta v_{cr})^2 \tag{3}$$

Where,

$$Z_r = \sqrt{L_r/C_r} \tag{4}$$

And by assuming that the converter is operating at 100% efficiency, so that all the power is passing via the resonant tank, the voltage swing at the capacitor is

$$\Delta v_{cr} = \frac{P_o T_s}{4nV_{in}C_r} \tag{5}$$

Finally, solving equations (2) and (3) at their intersection which is at the time $t_1 = d \cdot T_s$, the converter gain can be retrieved. The state plane trajectories are plotted in Fig. 4(a).

$$\frac{V_{out}}{nV_{in}} = M(d) = \frac{P_o T_s + \sqrt{(P_o T_s)^2 + 4P_o T_s V_{out}^2 C_r (1 - cos^2(\omega_r dT_s))}}{P_o T_s(cos(\omega_r dT_s) + 1)} \tag{6}$$

Greinacher Operation

In the Greinacher operation, S_5 is kept continuously in the ON state. In this state, the resonant capacitor voltage is DC biased, thereby extending the voltage gain of the converter. Like the other states, the primary bridge achieves ZVS turn-on and low current at their turn off times. S_6 can still achieve ZVS turn-on with the addition of an extra dead-time, and ZCS is achieved for D_2, while D_1 is not conducting any current during this operation.
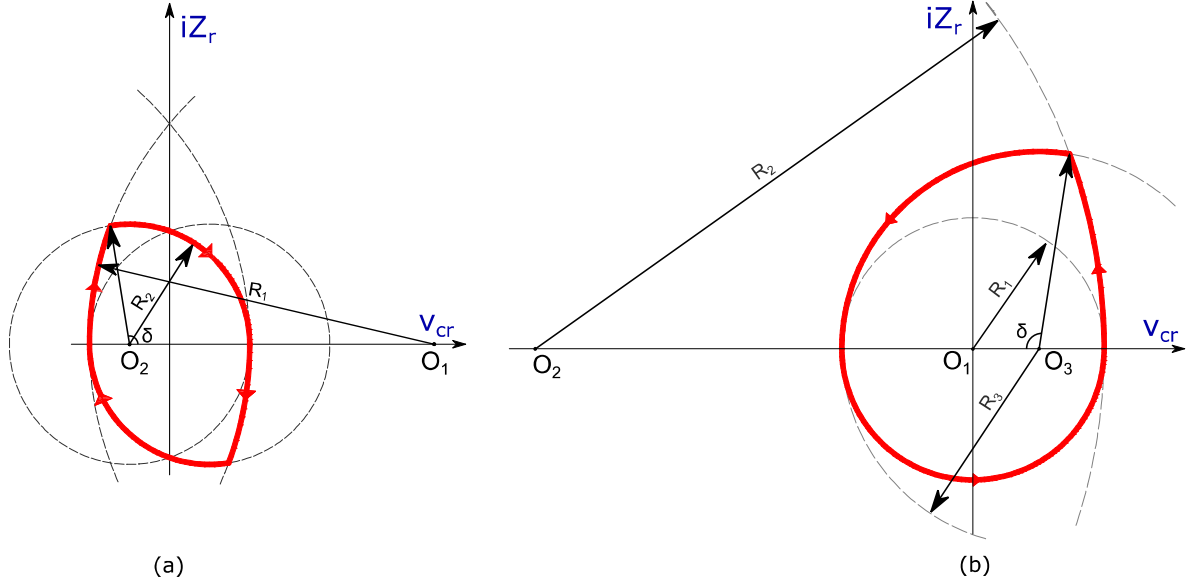
Fig. 4: State plane diagram of the resonant tank in the boosting mode (a) and at the Greinacher mode (b)

The DC biasing of the resonant capacitor using the charge balance equation is found to be equal to nV_{in}. Based on this fact, the gain of this mode can be found by solving for the state plane trajectories for the periods $t_0 - t_1$, and $t_1 - t_2$, and solving for their intersection point.

$$(v_{cr} + 2nV_{in})^2 + (Z_r i_{Lr})^2 = (2nV_{in} + \Delta v_{cr})^2 \tag{7}$$

$$(v_{cr} + 2nV_{in} - V_{out})^2 + (Z_r i_{Lr})^2 = (V_{out} - 2nV_{in} + \Delta v_{cr})^2 \tag{8}$$

$$M(d) = 2 \cdot \frac{nP_o T_s + \sqrt{(nP_o T_s)^2 + 2n^2 P_o T_s V_{out}^2 C_r (1 - \cos^2(\omega_r dT_s))}}{nP_o T_s (1 + \cos(\omega_r dT_s))} \tag{9}$$

Design of the Converter

To select an input capacitance, the criteria are the volume occupied by the capacitors, plus that the energy yield from the PV panel that must be kept high. A low capacitance would have a high voltage swing, therefore creating oscillations centered at the MPP, reducing the energy harvested from the panel. The desired capacitor value can be determined by the capacitor's charge equation, by setting the desired voltage swing and integrating the input current over half the switching period.

$$C_{in} = Q/\Delta v_{in} \tag{10}$$

To select the devices $S_1 - S_4$, apart from selecting a device with the required voltage rating, another consideration must be their performance. These devices will have ZVS turn-on and will be turning off with a moderate current, therefore the switching losses will be low, allowing for a potential silicon design. However, as silicon devices have increased parasitic capacitances, GaN FETs EPC2021 will be used to provide a design with a lower dead-time, and a lower gate driving loss.

For the design of the transformer turns ratio, it is designed to be close to the nominal voltage of the panel, which is taken to be a value typical for residential PV panels, equal to 35V, and the output high voltage side is taken as 380V.

$$n = V_{out}/V_{in,nom} \tag{11}$$

With the turn ratio decided, it is possible to design the transformer for maximum efficiency. The transformer core flux swing is equal to

$$\Delta B = \frac{V_{in}T_s}{4n_{pri}A_c} \tag{12}$$

And since the excitation of the transformer terminals is a square wave with minimal periods of zero voltage, the original Steinmetz equation gives an accurate result for the core loss [12].

$$P_{core} = k \cdot f^a \cdot B^\beta \tag{13}$$

For the core loss calculation, the ferrite N95 was used as it possesses a relatively flat loss to temperature curve [13], in the form factor of RM12. It is assumed the proximity effects on the wiring resistance will be minimal, as Litz wire will be used on the prototype, as well as interleaving to reduce the proximity effect in the primary side of the transformer, and a thinly stranded Litz wire is used on the secondary. Interleaving also brings the benefit of low leakage inductance, ameliorating the voltage stress that the primary devices will be under. Fig. 5 shows that the optimum number of primary turns is five, and for the secondary side, it is chosen that there will be 54 turns, to provide interleaving on the primary side, and give a total voltage step-up of $n = 10.8$.

(a)   (b)
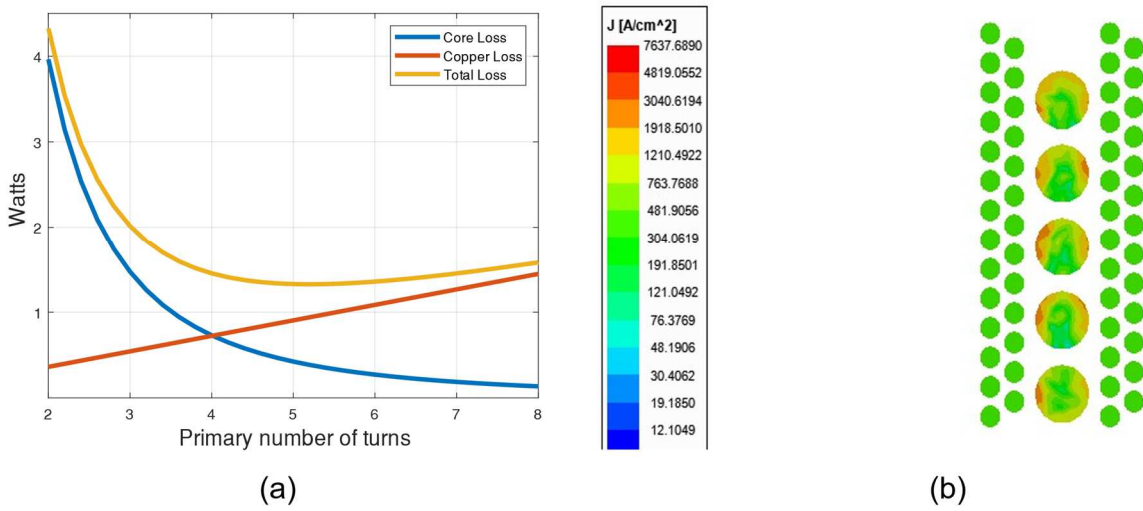
Fig. 5: Power losses of the transformer for different winding numbers(a), and the effects of balanced interleaving on a solid copper wire (b). It is seen that the current density does not gravitate towards a particular side in the middle (primary) conductors.

For the design of the air gap, utilizing equation (1), and setting the switching frequency equal to 140kHz gives

$$L_m \leq 54812 \cdot t_{dt} \tag{14}$$

And the transformer's magnetizing inductance may be controlled by adding an air gap approximated as

$$l_g = \frac{\mu_0 A_c n_{sec}}{L_m} \tag{15}$$

An air gap of $0.7mm$ was selected, which should give an approximate magnetizing inductance of $L_m = 658\mu H$, according to equation (15). The design is verified by Ansys Maxwell 3D simulation and experimentally. The transformer has been constructed with enameled copper wire to test the

resulting magnetizing and leakage inductances. The results were retrieved via the Keysight E4990A impedance analyzer with an AC voltage excitation at the switching frequency. By replacing the measured magnetizing inductance in Table I with equation (14), it is found that $t_{dt} > 13ns$. C_{oss} was calculated by integrating the $C_{oss} - V$ graph provided by EPC for their EPC2021 eFET from 0 to 35V and dividing by 35.

Table I: Simulated and measured transformer values

	Simulation	Experiment
$L_{leak,sec}$	9.42 μH	9.46 μH
$L_{m,sec}$	749.60 μH	701.19 μH
Coupling factor	99.3%	99.2%

Concerning the design of the resonant tank, a higher resonant inductor correlates with lower DCM periods, and therefore lower RMS currents and higher efficiency. However, DCM must be achieved in all operating regions to benefit from ZCS on the diodes and low current turn off on $S_1 - S_4$. This condition can be formulated geometrically from state plane diagrams (Fig. 4).

$$T_s/2 \geq dT_s + \delta/\omega_r \tag{16}$$

For the boosting operation, this equals to:

$$T_s/2 \geq dT_s + \sin^{-1}(R_1 \sin(\omega_r dT_s))/\omega_r \tag{17}$$

And for the Greinacher operation:

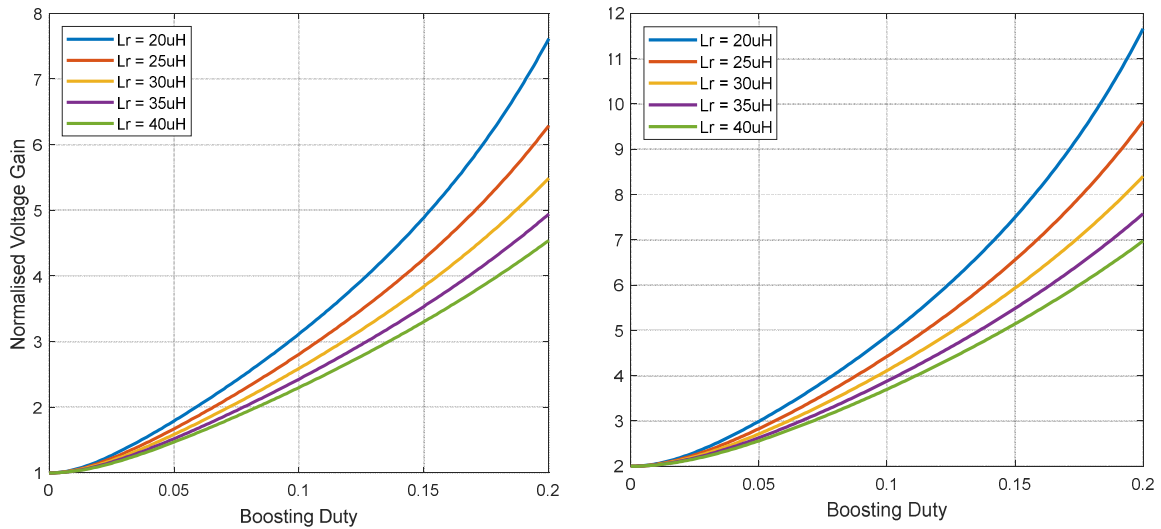$$T_s/2 \geq dT_s + \sin^{-1}(R_2 \sin(\omega_r dT_s))/\omega_r \tag{18}$$

Fig. 6: Widening of duty ratio in the boosting operation (left) and in Greinacher operation (right) at full load.

Nevertheless, an increased inductor also results in a widened duty cycle required for boosting the voltage, thereby increasing the turn-off loss of S_5, S_6 and the RMS currents converter wide. For this reason, the required voltage gain range must be set, and a duty cycle constraint set to select the resonant inductance. A voltage gain of 1-4 will be sufficient in controlling the PV panel to its MPP even in case of extreme shading where two bypass diodes are conducting, and the panel's output

voltage is derated by two thirds. Another restriction on the resonant tank is that the resonant capacitor may not exceed the output voltage, otherwise the converter will not operate as required. The limiting factor is greater in the Greinacher mode, as the capacitor is DC biased with nV_{in}. The capacitor should also be selected so that it does not have a large capacitance derating at DC biasing operation.

$$\frac{P_o T_s}{4nV_{in}C_r} + nV_{in} < V_{out} \tag{19}$$

Based on the above discussion, the resonant inductance is selected as $L_r = 40\mu H$, and the resonant capacitance is selected based on the resonance frequency being slightly higher than the switching frequency.

$$C_r \approx \frac{1}{L_r \omega_s} \tag{20}$$

For the design of S_5, S_6, the devices are selected based on their voltage rating, and their ability to perform a fast switch-off transition. For the diodes, similarly, the key metrics are the low conduction losses and sufficient voltage rating.

Simulation Results

The proposed converter was tested in PLECS 4.5.8, with the solar panel used being the FuturaSun FU 300M. The PV panel is modelled as a LUT with the simplified model presented by Bellini et al [14]. The converter is running at $f_s = 140kHz$. It is shown in Fig. 7 that the converter controls the PV panel voltage on the full designed range, and it reaches the desired voltage point in less than 5ms. One PI block is used to control the duty cycle, and a voltage sensor is attached to the panel to control the input voltage, as well as to change the control scheme at $M = 2$, which occurs at $V_{ref} = 17.5\,V$. At the transition point, the PI block is damped to avoid large currents due to the rapid duty cycle change.
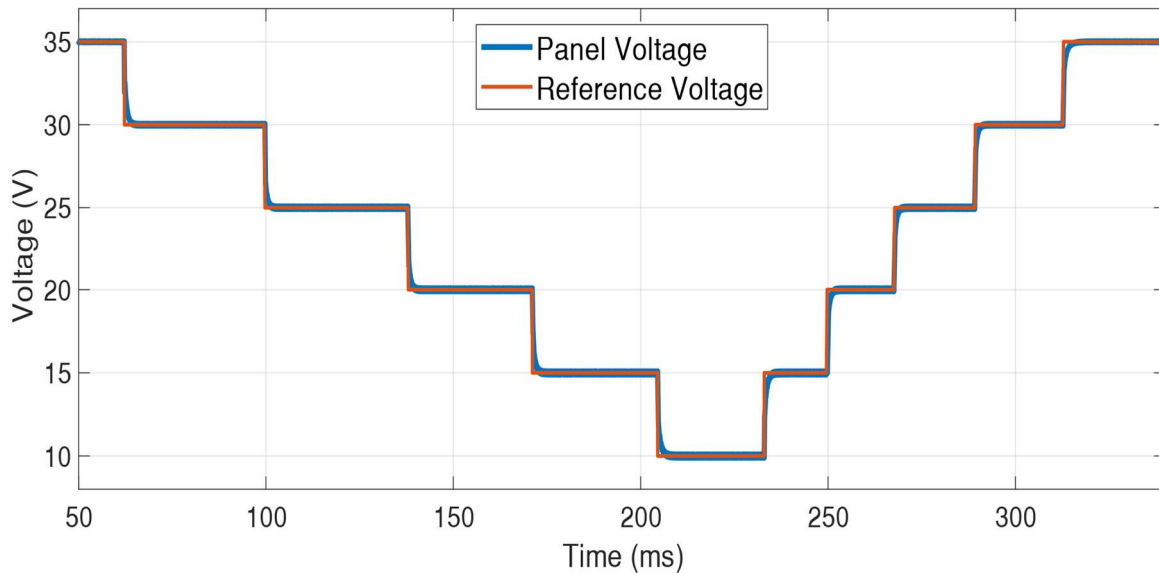

Fig. 7: PLECS model of the proposed topology. FU 300M is interfaced with a 380V DC bus.

Furthermore, the system was modelled using the PLECS thermal and magnetics domains, to estimate the converter's efficiency. The parameters used are summarized in Table II.

To calculate the losses, the data provided in the respective manufacturers' datasheet were used. For the switching losses, double pulse tests were run in LTSpice using manufacturer-provided SPICE models to estimate the switching transition time. The efficiency in different operating modes is shown in Fig. 8. In the partial shading condition, the power given by the PV will be less than the nominal, hence

from this figure, it is seen that the converter maintains high efficiency of over 90% over the controlled voltage range. The loss distribution is shown in Fig. 9 to demonstrate the impact of the increase in the gain ratio. The majority of the losses when the gain is increased arise from the copper losses in the transformer and inductor, as well as the turn off loss in S_5, S_6.
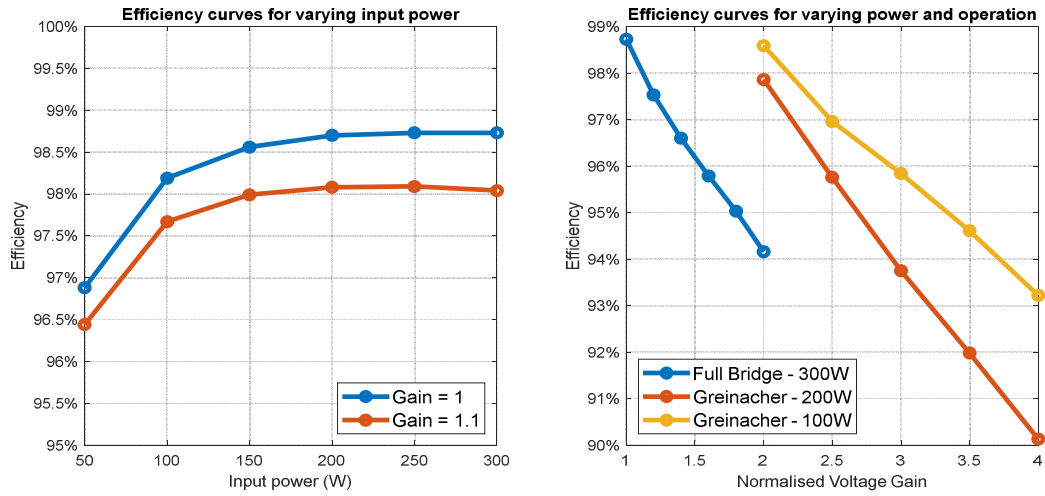

Fig. 8: Efficiency curves for varying PV power (left) and varying voltage gain (right).

Table II: Simulated components list

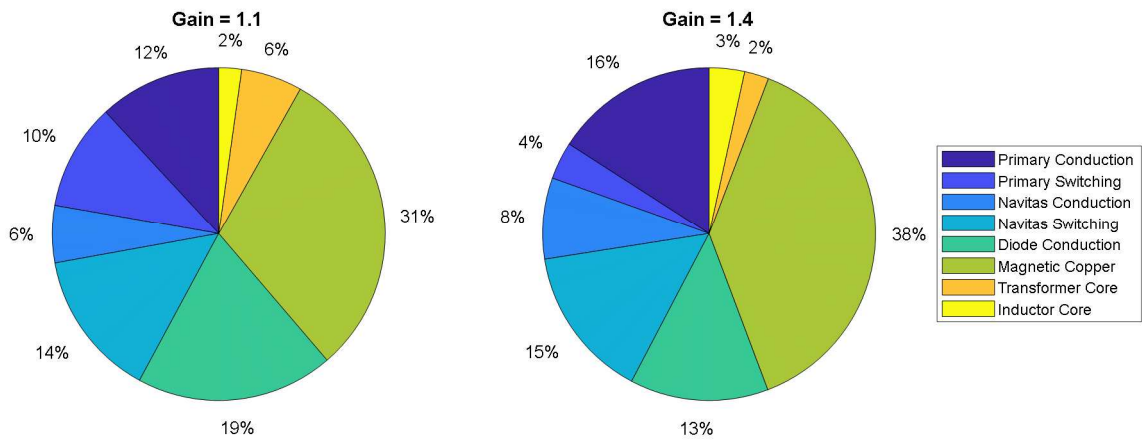| C_{in}:	$80\mu F$	$D_1 - D_2$:	C3D02060E
$S_1 - S_4$:	EPC 2021	L_r:	$40\mu H$
$S_5 - S_6$:	NV 6115	C_r:	$35nF$
Transformer Primary/Secondary coils:	5 turns: 435/40AWG/ 54 turns 300/46AWG	External Inductor:	14 turns 300/46AWG
Transformer Core:	N95/RM12, 0.7mm gap	Inductor Core:	N95/RM8, 0.5mm gap

Fig. 9: Loss distribution at gain 1.1 (left) and gain set to 1.4 (right) with power set to the nominal 300W.

Conclusion

A highly efficient isolated DC-DC converter was presented for the PV power optimizer application. The proposed converter can operate in a wide input voltage range, making it an excellent candidate for shade-tolerant PV power production. The design benefits from zero-voltage switching and zero-current switching based on its resonant design, but it is operating at a fixed frequency, thus curtailing the limitations frequency-modulated resonant converters have. Based on its low switching losses and low magnetics count, it is also a good candidate for high power density design, enabling future integration with PV modules directly.

References

[1] B. Subudhi and R. Pradhan, "A comparative study on maximum power point tracking techniques for photovoltaic power systems," IEEE Transactions on Sustainable Energy, vol. 4, no. 1, pp. 89–98, 2013, doi: 10.1109/TSTE.2012.2202294.

[2] K. Alluhaybi, I. Batarseh, and H. Hu, "Comprehensive Review and Comparison of Single-Phase Grid-Tied Photovoltaic Microinverters," IEEE Journal of Emerging and Selected Topics in Power Electronics, vol. 8, no. 2, pp. 1310–1329, Jun. 2020, doi: 10.1109/JESTPE.2019.2900413.

[3] A. Chub, D. Vinnikov, O. Korkh, M. Malinowski, and S. Kouro, "Ultra-Wide Voltage Gain Range Microconverter for Integration of Silicon and Thin-Film Photovoltaic Modules in DC Microgrids," IEEE Transactions on Power Electronics, pp. 1–1, 2021, doi: 10.1109/TPEL.2021.3084918.

[4] T. Labella, W. Yu, J. S. Lai, M. Senesky, and D. Anderson, "A bidirectional-switch-based wide-input range high-efficiency isolated resonant converter for photovoltaic applications," IEEE Transactions on Power Electronics, vol. 29, no. 7, pp. 3473–3484, Jul. 2014, doi: 10.1109/TPEL.2013.2282258.

[5] X. Zhao, C. W. Chen, and J. S. Lai, "A High-Efficiency Active-Boost-Rectifier-Based Converter with a Novel Double-Pulse Duty Cycle Modulation for PV to DC Microgrid Applications," IEEE Transactions on Power Electronics, vol. 34, no. 8, pp. 7462–7473, Aug. 2019, doi: 10.1109/TPEL.2018.2878225.

[6] A. Chub, D. Vinnikov, O. Korkh, T. Jalakas, and G. Demidova, "Wide-Range Operation of High Step-Up DC-DC Converters with Multimode Rectifiers," Electronics (Basel), vol. 10, no. 8, p. 914, Apr. 2021, doi: 10.3390/electronics10080914.

[7] Y. Wei, Q. Luo, and H. Alan Mantooth, "A Novel LLC Converter with Topology Morphing Control for Wide Input Voltage Range Application," IEEE Journal of Emerging and Selected Topics in Power Electronics, pp. 1–1, 2020, doi: 10.1109/JESTPE.2020.3044207.

[8] D. Vinnikov, A. Chub, E. Liivik, and I. Roasto, "High-Performance Quasi-Z-Source Series Resonant DC-DC Converter for Photovoltaic Module-Level Power Electronics Applications," IEEE Transactions on Power Electronics, vol. 32, no. 5, pp. 3634–3650, May 2017, doi: 10.1109/TPEL.2016.2591726.

[9] H. M. Maheri, S. S. Vala, A. B. Mirza, E. Babaei, and D. Vinnikov, "A Novel Extendable High Gain Step up DC-DC Converter," 2021 IEEE 62nd International Scientific Conference on Power and Electrical Engineering of Riga Technical University (RTUCON), pp. 1–6, Nov. 2021, doi: 10.1109/RTUCON53541.2021.9711745.

[10] S. B. Kjaer, J. K. Pedersen, and F. Blaabjerg, "A review of single-phase grid-connected inverters for photovoltaic modules," IEEE Transactions on Industry Applications, vol. 41, no. 5, pp. 1292–1306, Sep. 2005, doi: 10.1109/TIA.2005.853371.

[11] Y. Shen, H. Wang, Z. Shen, Y. Yang, and F. Blaabjerg, "A 1-MHz Series Resonant DC-DC Converter with a Dual-Mode Rectifier for PV Microinverters," IEEE Transactions on Power Electronics, vol. 34, no. 7, pp. 6544–6564, Jul. 2019, doi: 10.1109/TPEL.2018.2876346.

[12] J. Mühlethaler, J. Biela, J. W. Kolar, and A. Ecklebe, "Improved core-loss calculation for magnetic components employed in power electronic systems," IEEE Transactions on Power Electronics, vol. 27, no. 2, pp. 964–973, 2012, doi: 10.1109/TPEL.2011.2162252.

[13] "Ferrites and accessories SIFERRIT material N95," 2017.

[14] A. Bellini, S. Bifaretti, V. Iacovone, and C. Cornaro, "Simplified model of a photovoltaic module," in Applied Electronics, 2009, pp. 47–51.